

Large-scale structure formation for power spectra with broken scale invariance

R. Kates, V. Müller, S. Gottlöber, J.P. Mückel, J. Retzlaff

Astrophysikalisches Institut Potsdam, Germany

Accepted Received ; in original form 1995

ABSTRACT

We have simulated the formation of large-scale structure arising from COBE-normalized spectra computed by convolving a primordial double-inflation perturbation spectrum with the CDM transfer function. Due to the broken scale invariance ('BSI') characterizing the primordial perturbation spectrum, this model has less small-scale power than the (COBE-normalized) standard CDM model. The particle-mesh code (with 512^3 cells and 256^3 particles) includes a model for thermodynamic evolution of baryons in addition to the usual gravitational dynamics of dark matter. It provides an estimate of the local gas temperature. In particular, our galaxy-finding procedure seeks peaks in the distribution of gas that has cooled. It exploits the fact that "cold" particles trace visible matter better than average and thus provides a natural biasing mechanism. The basic picture of large-scale structure formation in the BSI model is the familiar hierarchical clustering scenario. We obtain particle in cell statistics, the galaxy correlation function, the cluster abundance and the cluster-cluster correlation function and statistics for large and small scale velocity fields. We also report here on a semi-quantitative study of the distribution of gas in different temperature ranges. Based on confrontation with observations and comparison with standard CDM, we conclude that the BSI scenario could represent a promising modification of the CDM picture capable of describing many details of large-scale structure formation.

Key words: primordial power spectrum – CDM – large-scale structure – galaxy clustering – cosmological velocity fields

1 INTRODUCTION

The search for a self-consistent model for the formation of large-scale structure capable of explaining the vast range of available observational data poses one of the greatest challenges in theoretical astrophysics. In this paper, we will present strong evidence that a large body of observations is consistent with a picture of structure formation based on a "double-inflationary" model (to be reviewed shortly). The most directly relevant observations include the measured large-scale anisotropy of the microwave background spectrum (Smoot et al. 1992, Górski et al. 1994), power spectra analysis of galaxy catalogs (Park et al. 1992, Vogeley et al. 1992, Fisher et al. 1993), count-in-cell analysis of galaxies (Efstathiou et al., 1990, Loveday et al. 1992), the galaxy correlation function based on IRAS, CfA, and other catalogs (Loveday et al. 1992, Vogeley et al. 1992, Baugh & Efstathiou 1993), the angular correlation function of APM galaxies (Maddox et al. 1990), abundance of clusters (Bahcall & Cen, 1993)) as a function of mass, rms line-of-sight peculiar relative velocity of galaxy pairs (Davis & Peebles,

1983, Mo et al. 1993). Other observational quantities include large-scale velocity fields in general, the line-of-sight distribution of quasar absorption clouds, X-ray observations giving information on the temperature and distribution of hot gas, the observed network of filaments and "walls", the existence of voids and their observed properties, and evidence for the epoch of galaxy and cluster formation.

Prior to the analysis of the APM catalog and the COBE measurement of the large-scale microwave anisotropy, the biased, σ_8 -normalized, flat CDM model (Blumenthal et al. 1982) was quite successful in predicting the observed hierarchical network of filaments, pancakes and nodes and observed galaxy clustering (White et al. 1987). Biasing, originally devised for explaining the enhanced correlation of Abell clusters (Kaiser 1984), also had the advantage of reducing small-scale velocity dispersions to reasonable levels. These advantages disappear with the COBE normalization of the CDM spectrum, because the antibiasing needed to explain the observed variances of counts in cells is quite difficult to reconcile with our observational knowledge of velocity fields and with other tests. More precisely: The normaliza-

tion fixed by the COBE anisotropy measurement appears to imply excessive power in the small-scale ($< 10h^{-1}\text{Mpc}$) regime of the primordial fluctuation spectrum $P(k)$, which manifests itself in various conflicts with observations. Predicted local velocity fluctuations seem to be quite in excess of measured relative pairwise line-of-sight projected velocities (Davis & Peebles 1983), although the measurements may be sensitive to sampling effects (Mo et al. 1993).

COBE-normalized (flat) CDM simulations also predict much more pronounced and numerous bound structures such as massive galaxies and galaxy clusters than observed (Efstathiou et al. 1992). Relative to these massive structures, COBE-normalized CDM appears to imply fewer galaxies in filamentary structures than would be expected from observations. In contrast, as we shall see, the double-inflationary models reproduce the observed filamentary structures rather easily and predict fewer massive galaxies and clusters. The different evolution of filamentary structures may be intuitively understood within the Zel'dovich (1970) picture of anisotropic collapse of overdense regions leading to the formation of pancakes on a broad range of scales. In particular, filaments are transitory structures: Due to the high normalisation, the COBE-normalized CDM is further developed, and therefore it is plausible that cooled material in filaments will have more time to flow into large clumps (compare Doroshkevich et al. 1995).

On the other hand, “tilted” models (compare e.g. Cen et al. 1993) seem to have insufficient small-scale power: as a consequence, the predicted epoch of galaxy formation is difficult to reconcile with the observation of high-redshift objects. Moderate-scale ($60h^{-1}\text{Mpc}$) power may also be too low, resulting in rather small streaming velocities. Mixed dark matter models (Davis et al. 1992, Klypin et al. 1993, Cen & Ostriker 1994) appear to agree better with a large body of observations, but again the late epoch of galaxy formation may be problematic (Mo & Miralda-Escudé, 1994, Kauffmann & Charlot, 1994).

Estimates of hot gas in clusters derived from X-ray observations seem to imply that a high percentage of the dynamical mass may be in the form of baryons. E.g., for the Coma cluster, White et al. (1994) compute that about 30 % of the dynamical mass is in the form of hot gas. If the estimate for $\Omega_b h^2 \approx 0.013$ obtained from nucleosynthesis is applicable in clusters (unless significant segregation of hot gas in clusters has occurred), then the total matter density in the universe would be restricted to the range $0.1 < \Omega < 0.3$. Indeed, low-mass CDM models (Kofman et al. 1993, Cen, Gnedin, & Ostriker 1993) with nonvanishing cosmological constant or low-mass and open CDM models (Kamionkowski et al. 1994) can explain the enhanced APM angular correlation function, probably the extended range of positive correlation of spatial galaxy correlation above $30h^{-1}\text{Mpc}$, the cluster mass function, and the cluster-cluster correlation function; however, the epoch of galaxy and cluster formation appears to be rather early. In particular, clusters in open models tend to be highly developed and tightly bound, exhibiting less substructure than observed (Kaiser 1991, Evrard et al., 1993).

In addition to strictly observational constraints, the theoretical appeal of a model and its consistency with our knowledge of particle physics also play an important role in its acceptance. Standard CDM was very appealing because it

involved only one true fit parameter (the amplitude of primordial fluctuations) together with one phenomenological parameter (biasing). “Low-mass” models are theoretically less attractive because they require a nonvanishing cosmological constant in order to achieve a flat universe, as preferred in an inflationary scenario. Tilted models introduce one additional parameter; however, the simplest scenario assuming an exponential inflaton potential is not theoretically well founded. Mixed dark matter models also involve only one additional parameter: (essentially) the neutrino mass (since their number density is fixed). The double-inflationary model requires two independent parameters. In Section 2, we review this model and describe fits to data in the linear regime (Gottlöber, Müller & Starobinsky 1991, GMS91; Gottlöber, Mücke & Starobinsky, 1994, GMS94) and in the Press-Schechter theory (Müller 1994a) resulting in the particular “BSI” (Broken Scale Invariance) spectrum studied in this paper.

Encouraged by the success of the BSI model in the linear regime, we now present the results of numerical n -body simulations in order to test observational results requiring accurate predictions in the nonlinear regime. Now, one of the subtleties of the nonlinear regime is that our incomplete understanding of physical processes at relevant length scales causes theoretical uncertainties that may be comparable to observational uncertainties (cp. for example, Ostriker 1993). Complicated, nonlinear feedback mechanisms govern the dynamics at scales below our numerical resolution. In particular, an adequate theory of galaxy formation (and perhaps evolution) together with significantly improved computational resources would obviate the necessity for introducing simple phenomenological concepts such as biasing. However, an accurate description of galaxy formation requires a robust treatment of gas dynamics over vast ranges of scales, densities, and other conditions; dynamic computation of heating and cooling, including thermal instability and ionization; star formation, supernovae; proper handling of the chemical evolution of a multi-component medium — to name a few considerations. Significant progress in applying a hydrodynamic approach to cosmology has been achieved by Katz & Gunn (1991), Navarro & Benz (1991), Cen & Ostriker (1992), Katz, Hernquist & Weinberg (1992), and by Steinmetz & Müller (1995). In particular, a hydrodynamical description is essential for studying the formation and internal dynamics of clusters (Evrard 1990). A comparative review containing additional references is now available (Kang et al. 1994). An alternative hydrodynamical approach emphasizing thermal instability and the importance of feedback mechanisms such as supernovae has been studied by Klypin, Kates & Khokhlov (1992; KKK92). Hydrodynamic simulations are clearly superior for obtaining reliable small-scale predictions from models of large-scale structure formation. However, a lack of computer resources still precludes their general use for high-resolution cosmological applications.

The numerical particle-mesh code used here (Kates et al. 1991, KKK91; Klypin & Kates 1992, KK) includes a model for thermodynamic evolution of baryons in addition to the usual gravitational dynamics of dark matter (see Section 3). The code provides an estimate of the (suitably averaged) local gas temperature without the enormous computational cost of a full hydrodynamical description. A resolution

of 512^3 cells (256^3 particles) was achieved. High resolution is crucial in the present study in order to include the effects of *both* enhanced large-scale power *and* modest (compared to CDM) small-scale power in the same simulation.

As discussed in Section 2, considerable preliminary testing using both linear analysis (compare GMS94) and moderate (256^3 cells) resolution (compare Gottlöber 1994, Müller 1994b, Amendola et al. 1995) was first carried out to obtain optimal estimates for the parameters k_{br} and Δ (see Section 2). These preliminary investigations also provided rough estimates of the sensitivity of our results to “fine-tuning” of parameters (see Conclusions), box size, etc. The power spectrum used in the highest-resolution simulations and its implementation in the numerical simulations will be given in Section 2.

Simulation of the coupling of thermodynamic evolution to gravitational dynamics provides us with important indirect information concerning observable quantities; see Section 4. In Section 5, we present our results on the evolution of the mass distribution and, in Section 6, its relationship to thermodynamic evolution. Of particular interest are the particle in cell fluctuations, the evolution of clustering with redshift and its dependence on the spectrum, redshift-dependence of thermodynamics and percentage of cooled particles, the relation between density peaks and hot and cold particles.

In Sections 7 and 8 we discuss the results of galaxy identification and galaxy clustering: galaxy mass function versus Press-Schechter theory; dependence on spectrum and redshift; galaxy correlation function versus correlation function of density peaks; clustering and other properties of galaxy clusters. The characteristic features of large- and small-scale velocity fields for BSI spectra are presented in Section 9. In Section 10, we draw our conclusions.

2 BSI POWER SPECTRUM

Standard inflation produces primordial adiabatic density perturbations $P(k) \propto k^n$ with a spectral index $n = 1$ plus small logarithmic corrections which stem from the slowly changing horizon length during inflation, i.e. they depend on the inflaton potential. We propose an early cosmological evolution which produces a power spectrum with a break at a characteristic scale by introducing more than one effective field responsible for inflation (Starobinsky, 1985). We use the combined action of renormalization corrections and a massive scalar field as the source of a non-flat primordial perturbation spectrum (GMS91). This model decouples the clustering properties at large and small scales. It requires two new parameters in addition to the amplitude: First, the ratio of the masses $\Delta \simeq m/(6.5M)$ appearing in the Lagrangian

$$L = \frac{1}{16\pi G} \left(R - \frac{R^2}{6M^2} \right) + \frac{1}{2} (\phi_\alpha \phi^\alpha - m^2 \phi^2); \quad (1)$$

this ratio essentially determines the ratio of power at small (galactic) scales to that at very large cosmic scales. Second, the epoch of the transition between inflationary phases is related to the initial energy density $m^2 \phi_0^2$ of the scalar field. This epoch determines a characteristic length scale $l_{br} \equiv 2\pi/k_{br}$ where the shape of the spectrum changes.

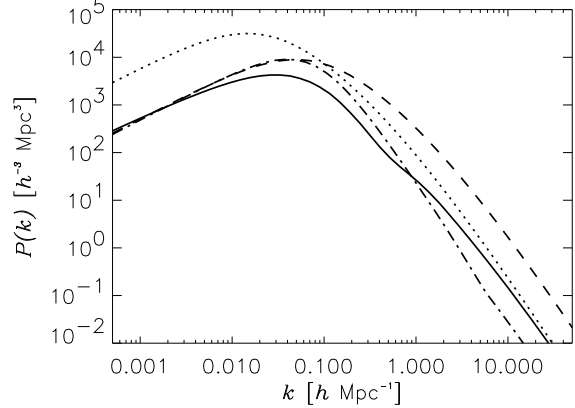


Figure 1. BSI power spectrum (solid line) compared with standard CDM (dashed line), a Λ CDM model (dotted line), and a MDM spectrum (dash-dotted line).

In GMS94, linear theory predictions of double-inflationary models were compared with observational constraints. Assuming COBE normalization, the tests applied were as follows: “counts in cells” of the IRAS and APM surveys, the APM galaxy angular correlation function, bulk-flow peculiar velocities, the Mach number test, and quasar abundance. The BSI models were shown to be in good agreement with all of these tests for the parameter regime defined by $2 \leq \Delta < 4$ and $0.5h^{-1}\text{Mpc} < k_{br}^{-1} < 5h^{-1}\text{Mpc}$, the latter corresponding to length scales $l_{br} \approx (3 - 30)h^{-1}\text{Mpc}$. Although some freedom is permitted by these constraints in the choice of k_{br} (or l_{br}), the best fit seems to be given by $k_{br}^{-1} = 1.5h^{-1}\text{Mpc}$, $\Delta = 3$. These values also led to reasonable effective biasing parameters in preliminary test simulations. In all simulation results reported here, the terminology “BSI spectrum” refers to these values of the parameters unless otherwise stated.

After convolution with the standard CDM transfer function of Bond & Efstathiou (1984), taking $\Omega = 1$ and $h = 0.5$, the power spectrum is used to generate the initial condition of the numerical simulations described in the next section. Fig. 1 plots the transformed BSI spectrum in comparison with the power spectra of the standard CDM model, a Λ CDM ($\lambda \equiv \Lambda/3H^2 = 0.8$, $\Omega = 0.2$) and an MDM model ($\Omega_{\text{CDM}} = 0.7$, $\Omega_\nu = 0.2$, $\Omega_b = 0.1$). The standard CDM spectrum has much more power at all the relevant scales for galaxy formation, while BSI mostly resembles MDM at large scales, but has more power on small scales, almost as high as the Λ CDM model. An analytical fit to the primordial potential spectrum is given by

$$k^3 \Phi(k) = \begin{cases} 4.2 \times 10^{-6} [\log(k_s/k)]^{0.6} + 4.7 \times 10^{-6} & (k \leq k_s) \\ 9.4 \times 10^{-8} \log(k_f/k) & (k > k_s) \end{cases} \quad (2)$$

with $k_s = (2\pi/24)h\text{Mpc}^{-1}$, $k_f = e^{56}h\text{Mpc}^{-1}$. However, for a proper representation of the transition regime, the numerically tabulated spectrum is preferable.

In Fig. 2 we show the predicted multipole moments of the anisotropies of CMB fluctuations calculated following Gottlöber & Mücke (1991) in comparison with new measurements on the angular scale $2 < l < 1200$. Our spec-

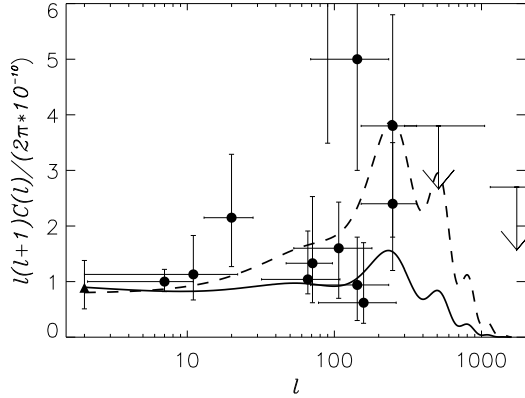


Figure 2. Comparison of the cosmic background fluctuation multipoles of BSI (solid line) and standard CDM (dashed line) with a series of experiments.

tra are normalized with the 10° -variance of the fluctuations $\sigma_T = (30 \pm 7.5) \mu\text{K}/2.735 \text{ K}$ from the COBE first-year data (Smoot et al. 1992). The triangle denotes the first-year COBE result $Q_{\text{rms-PS}} = (16.7 \pm 4) \mu\text{K}$ (for the spectral index $n = 1$) which is approximately equivalent to our normalization. The other experimental data (courtesy of B. Ratra, from Bond 1994) are from left to right COBE, FIRS, Tenerife, SP91, SK93, the lower end of the PYTHON error, ARGO, MAX1 and MAX2, full and source free MSAM2 and MSAM3, and the upper limits of WD and OVRO (for details see Bond 1994). The reanalysis of the COBE second-year data by Górski et al. (1994) implies an about 25 per cent higher normalization of the spectra (Gottlöber 1994). Consequences of such an increase will be discussed in the conclusions.

3 NUMERICAL REALIZATION

Initial fluctuations corresponding to BSI and standard CDM power spectra were generated as realizations of a Gaussian random field. Positions and velocities were assigned according to the Zel'dovich approximation at redshift $z = 25$ (although for larger boxes the Zel'dovich approximation could have been continued until a later epoch). The Euler-Poisson system describing the evolution of self-gravitating, collisionless matter was then evolved from $z = 25$ to $z = 0$ using the particle-mesh (PM) code described in KKK91 and KK.

To cover a large range of the spectra, we performed a series of simulations with different box sizes (see Table 1). Asterisks denote high resolution simulations (512^3 cells and 256^3 particles); the remainder of the simulations were performed using 256^3 cells and 128^3 particles. The two high-resolution BSI simulations were performed in boxes of $200h^{-1}\text{Mpc}$ and $25h^{-1}\text{Mpc}$. BSI-200* is intended for analysis of the large-scale matter distribution, while BSI-25* should provide good working accuracy on galactic scales. In order to highlight differences between BSI and standard CDM, a series of simulations with half of this resolution were performed using the same random seed in boxes of size $25h^{-1}\text{Mpc}$, $75h^{-1}\text{Mpc}$, $200h^{-1}\text{Mpc}$, and $500h^{-1}\text{Mpc}$.

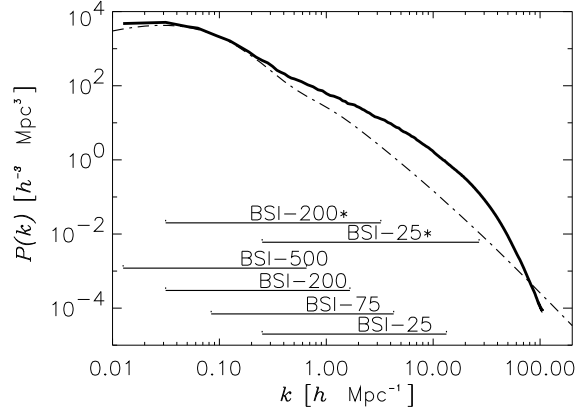


Figure 3. Range of spectra realized in the simulations BSI-25 – 500 (horizontal lines indicate k_{min} to k_{max}); also shown is the linear theory BSI spectrum (dash-dotted line) and a reconstruction assembled from the BSI simulations at $z = 0$ (full line).

l_{grid} gives the size of the particles used in the cloud-in-cell mass assignment scheme as well as the formal resolution of the grid on which the gravitational force is calculated. The Nyquist wavelength $2\pi/k_{\text{max}}$, which depends on the number of particles used in the simulation, is four times larger than l_{grid} . It corresponds to an upper limit for the realization of initial perturbations in k -space. M_{B+DM} is the total mass of a particle. Finally, we compare the grid variances of density contrast σ_δ and peculiar velocities σ_v of the initial realization of the Gaussian random field with the expectations of the linear power spectrum,

$$\tilde{\sigma}_\delta^2 = \frac{1}{2\pi^2} \int_{k_{\text{min}}}^{k_{\text{max}}} dk k^2 P(k), \quad \tilde{\sigma}_v^2 = \frac{H_0^2}{2\pi^2} \int_{k_{\text{min}}}^{k_{\text{max}}} dk P(k), \quad (3)$$

where the numbers are given at $z = 0$ transformed according to the linear theory growth law. They describe the quality of the realizations of the power spectra in the different simulation boxes.

On the scale of $8 h^{-1}\text{Mpc}$, one often refers to the measured unit variance of galaxy counts in spheres as determined from the CfA-catalog ((Davis & Peebles, 1983). Using the first integral of Eq. 3 with a top-hat window of radius $8 h^{-1}\text{Mpc}$, we infer $\sigma_\delta = 0.46$ for the BSI power spectrum. Therefore we predict a (linear) bias of galaxies with respect to dark matter of $b \approx 2.2$. For the standard CDM model we have on the other hand $\sigma_\delta^2 = 1.12$, i.e. there the galaxies should be slightly antibiased.

4 THERMODYNAMIC ESTIMATES OF GAS TEMPERATURES

As described in KKK91 and KK, estimates of the average values of the local dark matter density and velocity and of the local baryon temperature can be obtained from simulations of large-scale structure (without direct simulation of hydrodynamics) by following the thermal history of the gas while imagining that, smeared out over a sufficiently coarse

Table 1. Parameters of the simulations

| Simulation | l_{grid} [$h^{-1}\text{Mpc}$] | $M_{\text{B+DM}}$ [M_{\odot}] | σ_{δ} | $\tilde{\sigma}_{\delta}$ | σ_v [km s^{-1}] | $\tilde{\sigma}_v$ [km s^{-1}] |
|------------|---|--------------------------------------|-------------------|---------------------------|--------------------------------------|--|
| BSI-200* | 0.39 | 2.6×10^{11} | 2.28 | 2.25 | 490 | 483 |
| BSI-25* | 0.05 | 5.2×10^{08} | 4.60 | 4.69 | 223 | 219 |
| BSI-500 | 1.95 | 3.3×10^{13} | 0.94 | 0.93 | 512 | 508 |
| CDM-500 | 1.95 | 3.3×10^{13} | 3.02 | 2.99 | 1049 | 1040 |
| BSI-200 | 0.78 | 2.1×10^{12} | 1.62 | 1.60 | 516 | 479 |
| CDM-200 | 0.78 | 2.1×10^{12} | 5.43 | 5.36 | 1103 | 1068 |
| BSI-75 | 0.29 | 1.1×10^{11} | 2.59 | 2.54 | 441 | 376 |
| CDM-75 | 0.29 | 1.1×10^{11} | 8.79 | 8.65 | 1064 | 979 |
| BSI-25 | 0.10 | 4.1×10^{09} | 3.85 | 3.76 | 269 | 219 |
| CDM-25 | 0.10 | 4.1×10^{09} | 13.1 | 12.8 | 857 | 735 |

scale, baryons are transported with the dark matter; i.e., $\rho_{\text{gas}} \equiv \rho\Omega_b$, where $\Omega_b = 0.1$ is the background fraction of baryons. The practical advantage of this picture is that the thermal history of the gas reduces to integration of one or more ordinary differential equations along *known* trajectories (those of the dark matter).

This description is certainly unproblematic before the formation of the first shocks, when the medium is still cold and fluctuations are small (we put $T_{\text{gas}} = 0$ at $z_{\text{start}} = 25$). As perturbations grow, eventually the first objects start to collapse, producing caustics in the dark matter and shocks in the gas. As simple pancake models show (Shapiro & Struck-Marcell 1985), shocks occur close to caustics.

The label “shocked” may be assigned to a particle in one of two ways: First, particles for which the Jacobian determinant of the transformation from Lagrangian to Eulerian coordinates is negative are classified as shocked. (Particle labels (i, j, k) are the numerical realization of Lagrangian coordinates. The position assigned to a particle is the numerical representation of its Eulerian coordinates.) The Jacobian is determined for each particle by considering the volume element constructed from the position vectors to its nearest Lagrangian neighbors. Second, a particle inherits the label “shocked” by passing through a shocked region. More precisely, if particle (i, j, k) is in cell (I, J, K) , then the label shocked is assigned to particle (i, j, k) if the density of previously shocked gas is nonzero in cell (I, J, K) and all neighboring cells.

At a shock, the temperature acquired by gas particles with velocity \vec{v} is given by

$$kT \approx \mu_M m_H (\vec{v} - \vec{U})^2 / 3, \quad (4)$$

where \vec{U} is the local velocity determined by interpolation of the velocity field onto a coarse grid of twice the usual cell size. (If it should happen that too few particles are present to determine \vec{U} , the temperature assignment is simply postponed.) This estimate is relatively insensitive to small errors in the position of the shock. Here, m_H is the mass of hydrogen, and μ_M is the molecular weight per particle, $\mu_M \approx (n_H + 4n_{He}) / (2n_H + 3n_{He}) \approx 0.6$.

When a particle crosses a shock and is assigned a temperature, we start to integrate the energy equation along the trajectory of the particle:

$$\frac{dT}{dt} = (\gamma - 1) \left(\frac{T}{n_H} \frac{dn_H}{dt} - \frac{\mu_M}{\mu_H} \frac{1}{kn_H} (\Lambda_{\text{rad}} + \Lambda_{\text{Comp}}) \right), \quad (5)$$

where μ_H is the molecular weight per hydrogen atom, $\mu_H \approx (n_H + 4n_{He}) / n_H \approx 1.4$, $\rho_{\text{gas}} \equiv \rho\Omega_b = n_H \mu_H m_H$, and $\gamma = 5/3$. Here, Λ_{rad} represents radiative losses in the hot plasma with assumed primordial abundances, and Λ_{Comp} is the cooling rate due to Compton scattering. To estimate Λ_{rad} , we used analytic fits as in KK and KKK91 to the cooling curves given in Fall & Rees (1985). The medium is treated as optically thin and in collisional equilibrium.

Computation of the increment in T due to the (Lagrangian) time derivative of n_H in Eq. 5 requires a knowledge of n_H at the present and at the previous timestep. For each timestep, we construct the “gas density” on the grid, defined by counting only contributions of shocked (hot) particles. (For the dark matter density, one of course counts all particles). For the evolution of Eq. 5, the present value of n_H for Eq. 5 is computed simply by interpolation to the position of the particle and then stored for use at the following timestep.

Now, when material cools below 10^4 K, stars will form, producing luminous matter. By assigning the label “cooled” to the particles with $T < 10^4$ K, we have a measure for the amount of visible matter. However, we know that the efficiency for the conversion of gas to stars is low. One nonlinear feedback mechanism limiting star formation could be the energy provided to the medium by supernova explosions. A second (also nonlinear) mechanism inhibiting star formation is ionization and heating due to ambient ultraviolet radiation. As emphasized by Efstathiou (1992), a similar mechanism could be responsible for suppressing the formation of dwarf galaxies. It should be emphasized that *some* mechanism preventing conversion of the gas to luminous matter is necessary in BSI models as well as in CDM and in the pre-COBE version of CDM: otherwise, all the gas would simply collapse, forming stars and ending up in globular clusters long before the formation of large objects.

In the present realization of the code, we take these effects into account in a crude and purely local manner: we “reheat” those particles to the temperature $T_{\text{reheat}} = 5 \times 10^4$ K which have cooled to below 10^4 K with a probability P_{reheat} and assign to the remaining particles the label “cooled.” Some of the reheated particles later will attain high temperatures, provided they enter collapsing regions of high density. Reheated particles can simply cool again and turn into “visible” matter. However, once cooled, a particle cannot be reshocked. The value P_{reheat} was held constant at 85 per cent, the value estimated in KK for a $50 h^{-1}\text{Mpc}$

grid and a σ_8 normalized CDM spectrum to give a reasonable fraction of hot gas in clumps of galactic mass (about 10 per cent). The fraction of cooled gas (88 per cent) for a cell size of about $0.05h^{-1}\text{Mpc}$ in the highest resolution BSI simulation seems to be reasonable. The distribution of particles of different temperature ranges, variation with cell size and spectrum, and related considerations will be discussed below in Section 6.

We recall that the mean density of stars (and other components of the baryonic matter) in some comoving cell depends in principle on the entire past history of the cell and not just on its density at some particular epoch. As discussed in KKK91 and KK, comparison of the density distribution of “cold” material – which is related to the density of visible matter – with the dark-matter density thus yields information useful for testing cooling as a physical mechanism for “biased galaxy formation.”

A reasonable *upper* bound for the aforementioned “coarse graining” (i.e., error in predicting positions of baryons) is the local sound velocity integrated over a Hubble time (e.g., for $T \approx 5 \times 10^6$ K it is 2 or $3h^{-1}\text{Mpc}$). However, in tests – leaving aside conditions prevailing in clusters – for a box of $75h^{-1}\text{Mpc}$ (cell length $200h^{-1}\text{kpc}$), the error seems to be of the order of the cell resolution only. The explanation seems to be that both components move in the same potential well. The dark matter spends a large fraction of its time at about the same radius as the gas, because they originally had the same kinetic energy. Due to mixing, the dynamics of dark matter particles bears some resemblance to the dynamics of a gas whose temperature corresponds to the local velocity dispersion. Incidentally, from experiments with truncated spectra in KKK91 and from theoretical considerations, we know that temperature predictions are somewhat sensitive to the portion of the spectrum actually simulated. This fact implies that the same spectrum simulated in boxes of varying sizes can yield varying estimates of temperature distributions.

Results of a 1D-pancake test presented in KKK91 show good agreement of our model with hydrodynamical simulations (20 per cent of gas cooled, position of cooling front and shock wave). Proper inclusion of hydrodynamics and the effects of thermal instability would be expected to make a significant difference in at least two situations: First, when gas starts to cool efficiently – this happens inside dense regions and/or if the temperature becomes too low ($T < 2 \times 10^5$ K). Second, when gas undergoes secondary shocking – for example, in collapse to objects with masses smaller than a galactic mass (for more detailed comparison, see, KKK92). Thus, the code does not properly treat the internal regions of galaxies and clusters, but it would be expected to give a reasonable approximation for the temperature and distribution of gas which leaves voids and is trapped in the potential wells of superclusters and filaments. Comparison with Cen & Ostriker (1992) supports this expectation: the baryonic and dark matter distributions look remarkably similar; most of the gas in regions with density $\rho > 10\langle\rho\rangle$ has a temperature between 10^6 K and 10^7 K, similarly to what was found in KK. Comparison with hydrodynamic simulations of periodic disturbances reported in KKK92 also lead to reasonable qualitative agreement in this regime.

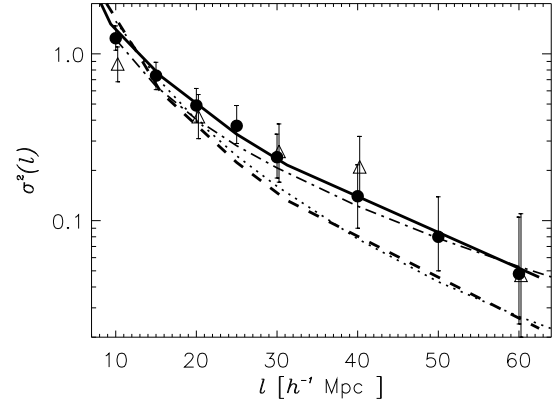


Figure 4. Comparison of the variances of counts in cells of galaxies of the Stromlo-APM (full circles) and IRAS (triangles) survey with the variances of the dark matter particles in the simulations. The BSI curve (solid line) composed from the simulations with different box sizes fits the data quite well. The dashed line corresponds to the CDM simulations. Dashed-dotted and dotted lines are the linear theory predictions of BSI and CDM, respectively.

5 COUNT-IN-CELL ANALYSIS FOR DARK MATTER

One useful method of characterizing the dynamics of clustering is to study the statistics of counts in cells. It is a robust measure for distinguishing different power spectra. For example, the rms fluctuations of simulated dark matter particles in a sphere of radius $8h^{-1}\text{Mpc}$ are often used to determine the linear biasing factor. The fluctuations on the scale of a galactic halo provide an estimate of the threshold density contrast required in galaxy identification algorithms. Comparison of the simulated count fluctuations as a function of radius with rms fluctuations observed in the IRAS catalog (Efsthathiou et al. 1990a) and the Stromlo-APM survey (Loveday et al. 1992) provides an important test of models.

In Fig. 4 the curves representing COBE-normalized BSI have been shifted vertically by a “biasing” factor $b_{\text{BSI}} = 2$ in order to normalize fluctuations to observations at $8h^{-1}\text{Mpc}$, while the CDM curves had $b_{\text{CDM}} = 0.9$. CDM fluctuations are too low (significantly outside the $1\text{-}\sigma$ error range on the low side) on scales $(15 - 50)h^{-1}\text{Mpc}$, after which the measurement errors increase. In contrast, the interpolation curves in the range of BSI simulations fit the data quite well. The good fit beyond about $15h^{-1}\text{Mpc}$ is consistent with the predictions of linear analysis (GMS94). The slight differences at small scales are due to the difference between linear and nonlinear evolution. The variances of cell counts are calculated in real space. At the scales studied the linear theory predicts a constant amplification factor which can be incorporated in the value of the bias parameter. The measured variances provide a good test of the slope of the BSI power spectrum. In contrast, the CDM counts in cells are inconsistent with observations at about the $2\text{-}\sigma$ level.

The redshift dependence of the probability distribution of particle-in-cell counts delivers an estimate of the non-linearity of clustering. Using the counts on a 128^3 grid of the $200h^{-1}\text{Mpc}$ -simulations, we compare BSI and CDM simulations in Fig. 5. Over four decades in the probability

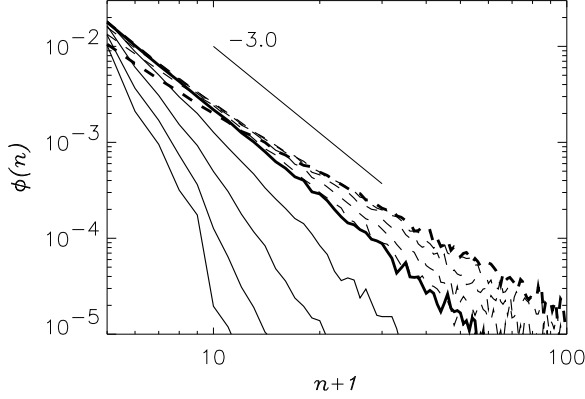


Figure 5. Particle-in-cell distribution of BSI-200 (full lines) and CDM-200 (dashed lines) simulations. The curves ($z = 2, 1.5, 1, 0.5, 0$) show the dependence of the probability distribution of grid cells on the number of particles in the cell; the curves are steeper at higher redshift. For reference, a curve of slope -3 is drawn, corresponding to an evolved stage of pancake formation.

it is remarkably well described by a power law $\phi(n) \propto n^{-3}$, which is a prediction of the pancake model (Kofman et al. 1993). The CDM models at $z = 0$ are less steep, corresponding to more big clumps in the matter distribution. The CDM models at about $z = 2$ had a similar slope to the BSI model at $z = 0$. The subsequent evolution to a less rapid fall off is a quantitative measure of the substantially increased clustering of CDM compared to BSI models. The large dynamical range of the dark-matter probability distribution as computed using the simulation cells is more of theoretical interest, and it cannot be compared directly with the one-point distribution function estimated from galaxy surveys.

6 GAS TEMPERATURES: STATISTICS AND SPATIAL STRUCTURE

As explained in Section 4, the “temperature” assigned to each particle depends on its complete history, including the epoch and conditions under which it was shocked and the environment (in particular the local density) at all intermediate times since shocking. At a particular time, say $z = 0$, the gas temperature distribution thus contains more information than the density and velocity distributions alone.

In interpreting the numerically computed gas temperature distribution, one should keep in mind the idealizations and limitations involved. As discussed above, a proper hydrodynamic treatment of the gas would be expected to make a systematic difference in regions with secondary shocking and/or very high density, in particular inside clusters and galaxies. However, any treatment of the gas, even including hydrodynamics, will contain numerical inaccuracies (resulting both from limited resolution and from systematic errors) as well as theoretical uncertainties due to incomplete modelling. Bearing all of these errors and uncertainties in mind, we take a brief look at what can be learned from particle temperature statistics.

In Fig. 6, the percentage of particles in selected temperature ranges at $z = 0$ for BSI and CDM simulations is plot-

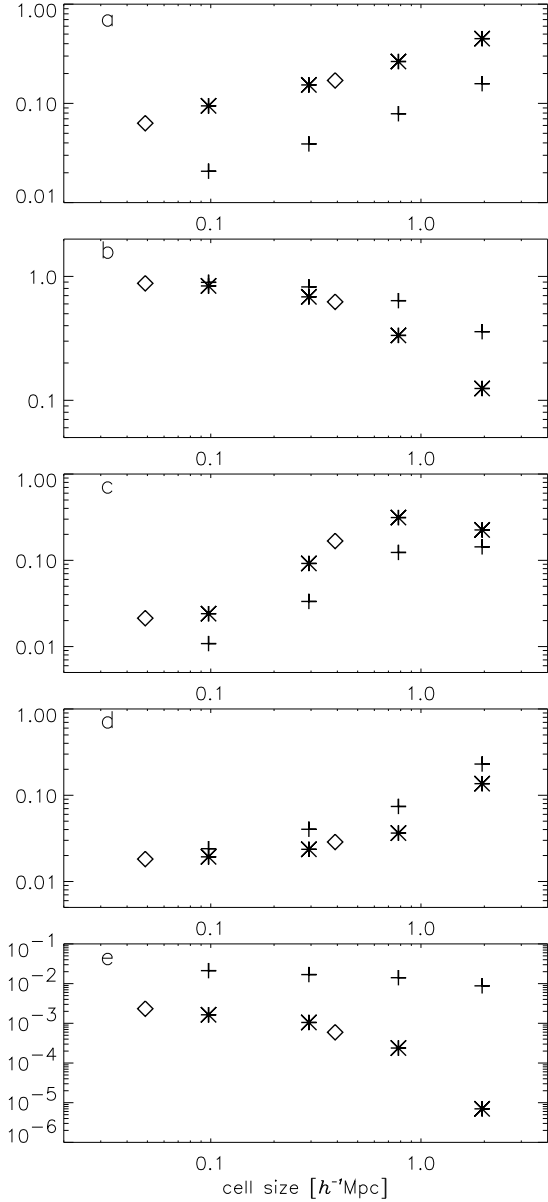


Figure 6. Percentage of particles in different temperature ranges as a function of *cell size* at redshift $z = 0$. Plus signs indicate CDM simulations, asterisks BSI, and diamonds high-resolution (512³ cells) BSI simulations. a) never shocked, b) cooled, c) temperature range $10^4 < T < 5 \times 10^4$, d) temperature range $10^5 < T < 1.5 \times 10^6$, e) temperature range $T > 10^7$.

ted against cell size, which for all simulations shown is inversely proportional to the highest resolved wavenumber. Indeed, studies of truncated spectra in high-resolution simulations (KKK91) indicate that the wavenumber limit is crucial to temperature statistics, i.e., qualitatively similar trends would be observed even if the spatial resolution were to be improved while keeping the wavenumber limit constant. (Incidentally, percentages do not add up to one, because the temperature ranges shown are not exhaustive.) Plus signs indicate CDM simulations, asterisks and diamonds BSI; diamonds indicate the high-resolution simulations, in which the ratio of highest to lowest resolved wavenumber is twice

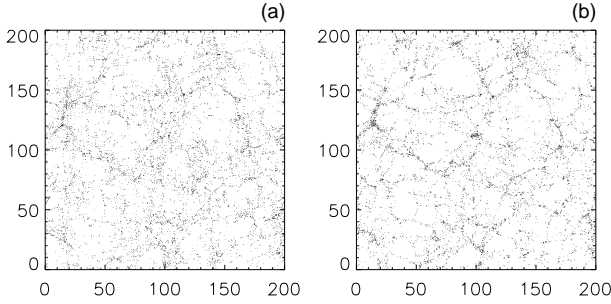


Figure 7. Comparison of slices through $200h^{-1}\text{Mpc}$ BSI (a) and CDM (b) simulations in the temperature range $10^4 \text{ K} < T < 5 \times 10^4 \text{ K}$.

as large. One expects the (limited) spectral range to have an influence on gas temperature statistics, and this expectation is borne out in Fig. 6. The trend with respect to cell size is different in different temperature ranges. However, the most striking regularity is that in all temperature regimes, a smooth (in most cases monotonic) trend is apparent upon plotting percentage against *cell* size (equivalently here: *highest* resolved wavenumber) rather than *box* size (equivalently here: *lowest* resolved wavenumber). A plot with respect to box size would be obtained by shifting the high-resolution points (diamonds) by one point to the right, which in all cases would move them off an otherwise smooth curve.

Fig. 7 illustrates a typical slice in the range $10^4 \text{ K} < T < 5 \times 10^4 \text{ K}$ for both BSI and CDM simulations. (Note that the random seed used in BSI and CDM simulations was the same, resulting in the same phase relations for each perturbation mode.) Slices are about $12h^{-1}\text{Mpc}$ thick. About 9000 particles are plotted in each slice (all of the particles in the CDM slice and about 40 per cent of the particles in the BSI slice). In Fig. 8, spatial distributions for BSI simulations are illustrated in the same thin slice for particles in the ranges $10^5 \text{ K} < T < 1.5 \times 10^6 \text{ K}$, $T > 10^7 \text{ K}$, cooled ($T < 10^4 \text{ K}$), and never shocked. The different temperature ranges highlight quite different features of the distribution in a way that would not be possible using simple peak statistics.

We now consider various temperature ranges in detail:

Never shocked: This percentage is a measure of the fraction of particles not in pancakes. The fraction increases monotonically with cell size for both BSI and CDM (Fig. 6a). The trend may be attributable to the fact that for larger cell size, the portion of the spectrum actually simulated is shifted toward smaller wavenumbers, with correspondingly smaller values of $k^3 P(k)$, resulting in longer timescales for formation of structures such as pancakes. The number of unshocked particles is consistently lower by a factor of about three for CDM than for BSI, directly reflecting the significantly enhanced small and medium-scale power of CDM compared to BSI. In Fig. 8a, the spatial distribution of unshocked particles is shown for a $25h^{-1}\text{Mpc}$ high-resolution simulation. The distribution shows practically no structure, aside from being absent in regions of high density, where all of the particles are shocked. Visual inspection of slices confirms one’s expectation that material in voids consists mainly of unshocked particles.

Cooled: From plausibility arguments one expects the distribution of “cooled” particles to trace the galaxy (halo) distribution more accurately than does the unbiased dark-matter distribution. (A higher probability of cold gas obviously favors star formation.) The results of KKK91 in the context of high-resolution, 2D simulations lend additional support to this expectation: There, halos were found with high confidence by a (“friends-to-friends”) clustering algorithm applied to *all* particles. The percentage of cold particles inside halos was significantly higher than outside. Moreover, the epoch of galaxy formation (estimated by cluster analysis at various redshifts) agreed with the average redshift z_{gal} at which the cold particles in galaxies “cooled.” In three dimensions, we exploit the affinity of cooled particles for galaxies in our galaxy-finding routines: As discussed in Section 7, the routines begin by searching for peaks in the cooled-particle distribution.

As seen in Fig. 6b, the percentage of cooled particles at $z = 0$ varies strongly with cell length (more precisely, with Nyquist frequency), mainly because power at smaller length scales leads to early formation of small pancakes and, in spite of “reheating,” subsequent cooling. (The redshift at cooling is recorded for each cooled particle.) Consider a structure of characteristic size L . Smaller structures are associated on the average with smaller characteristic initial temperatures ($\propto L^2$, since typical relative velocities in Eq. 4 scale with $H_0 L$). The CDM simulations have more small-scale power and therefore consistently fewer unshocked particles and more cooled particles. In KKK91, it was shown that truncation of the spectrum below the Nyquist frequency leads to significant reduction of the number of cooled particles (keeping spatial resolution constant). Thus, as in the case of unshocked particles, the variations with “cell size” seen here can probably be attributed to changes in the range of the spectrum actually simulated. Filaments and voids are evident in the cold particle distribution; the hierarchy of filament separations and void sizes give the visual impression of a broad distribution of characteristic length scales.

Particles in the temperature range $(1 - 5) \times 10^4 \text{ K}$:

This temperature range would tend to be associated with Lyman- α clouds. However, a more realistic treatment of the effect of the ultraviolet background on the matter (including ionization and heating) would be required to draw quantitative conclusions concerning Lyman- α clouds. Such a treatment is discussed by (Mückel et al. 1995). Nevertheless, we may obtain some hints as to what to expect from a more realistic treatment by examining the trend in Figs. 6c. The fraction grows monotonically both in BSI and in CDM with cell scale, except for the $500h^{-1}\text{Mpc}$ BSI simulation, with CDM consistently lower. A reasonable interpretation may be that earlier pancake formation and efficient cooling at moderate redshifts in the present code deplete the reservoir of particles (especially those near galaxies) that would otherwise be candidates for this temperature range. The turnover of the BSI curve at large scales is not surprising, since at the largest scales, the reservoir of shocked particles sets the limit. (In any case, quantitative studies of Lyman- α clouds would require resolution of about $50 - 100 \text{ kpc}$.)

With proper treatment of ionization and heating, the relative fraction of cold particles would be expected to drop significantly in favor of particles in the range of temperatures $(1 - 5) \times 10^4 \text{ K}$, except in very dense regions. Upon

examination of numerous slices, there is the visual impression that particles in the temperature range $(1 - 5) \times 10^4$ K at least roughly trace the distribution of cold particles at $z = 0$. This may be a hint that a population of Lyman- α clouds could be associated with galaxies (cp. Petitjean et al. 1995).

Comparing BSI and CDM slices for the temperature range considered in Fig. 7, there is a strong impression of thinner, better defined filaments and emptier voids in CDM than in BSI simulations. (Note that the total number of particles is the same.) This impression is consistent with the interpretation that the standard CDM looks like the BSI model would look like if it were evolved to a larger fluctuation amplitude.

Particles in the temperature range 10^5 K $< T < 1.5 \times 10^6$ K: As explained in KK, there are strong theoretical and observational reasons for an association between gas in this “warm” temperature range and filamentary structures. In Fig. 8c, it is evident that warm particles trace filaments quite closely in BSI. The same qualitative picture is found in all boxes. Comparison of CDM and BSI simulations in this warm regime shows little qualitative difference in filamentary structures, except that CDM consistently leads to somewhat more gas in the warm regime than BSI. This occurs despite CDM’s enhanced accumulation of material in clusters, which would tend to transfer gas from the warm to the hot regime (see discussion of hot gas below). The trend toward more warm gas at larger simulations may be related both to the increased reservoir of shocked, but not yet cooled particles (an essentially small-scale effect) and perhaps the influence of large-scale power in the portion of the spectrum actually simulated. This second cause is consistent with a rise just visible in the BSI curve at cell-size $0.39h^{-1}\text{Mpc}$ (high-resolution simulation).

Particles in the temperature range $T > 10^7$ K: The “hot” gas represented by these particles is generally associated with the deep potential wells of clusters, and therefore it is no surprise that in Fig. 8d hot gas traces clusters (also verified by comparison with galaxy catalogs). The percentage of “hot” particles with $T > 10^7$ K, which are nearly all associated with clusters or large galaxy groups, is consistently an order of magnitude higher for CDM than for BSI, the trend becoming even stronger at larger cell size. This trend is consistent with the general conclusion that CDM causes more and larger massive structures (also evident in slices). Moreover, these structures seem to be farther evolved in CDM, so that deep potential wells would also tend to be broader. Broader cluster potential wells would explain why the disparity between CDM and BSI grows at larger cell lengths (Fig. 6e). Cluster potential wells are still fairly well resolved at the poorest resolution in CDM, but not in BSI.

7 GALAXY IDENTIFICATION AND STATISTICS

The galaxy finding procedure used here was a modified density peak prescription: Based on the results of KKK91, KK, cooled particles are preferred tracers of the galaxy distribution. We therefore began by searching for local maxima of the density field of cold particles exceeding a predetermined threshold value δ_{th} . (The local maxima were also required

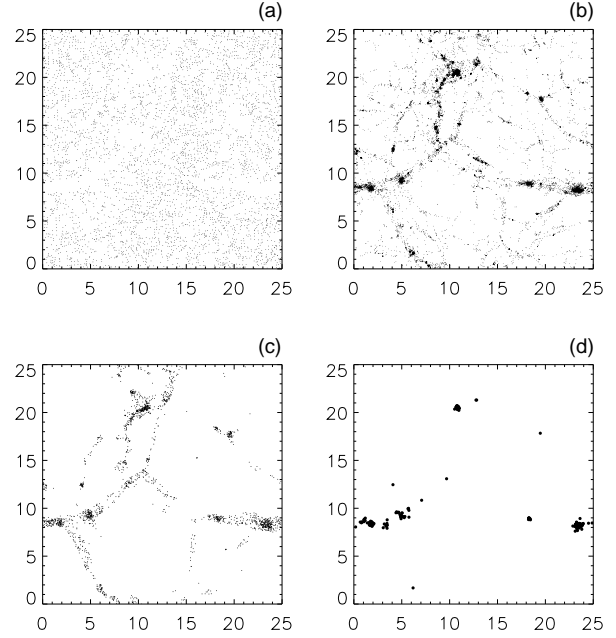


Figure 8. Slices of BSI-25* simulation at $z=0$. a) unshocked; b) cooled; c) 10^5 K $< T < 1.5 \times 10^6$ K; d) $T > 10^7$ K.

to be maxima within a 5^3 cell neighborhood.) The mass of the corresponding galaxy was then computed by summing the contributions of *all* particles within 0.5 cell lengths of the maximum in the lower resolution simulations and within one cell lengths of the maximum in the high resolution simulations. This leads to the same physical length for selecting halos in simulations of the same box size, i.e. to comparable catalogues. Since the centroid can shift due to addition of new particles, the procedure was iterated six times, and a centroid, velocity, and mass were assigned to the galaxy. For each simulation, several galaxy catalogs were constructed using various choices of threshold. Appropriate choices lie in the range $\delta_{\text{th}} = (1.5 - 3)\sigma_\delta$. In the end, one seeks a catalog including at least as many galaxies as would be expected from observational counts of galaxies with luminosities exceeding the characteristic Schechter luminosity L_* in the given volume. For numerical simulations, the mass corresponding to “ L_* ”-galaxies can only be determined from this requirement *a posteriori*. We observed that reducing the threshold simply resulted in including additional galaxies at the low end of the mass spectrum, but had virtually no effect on the galaxies at higher masses. Thus we can extract one big galaxy catalog from each simulation, which can be cut off at the low-mass end as required. A natural cut-off is implied by the finite resolution of the simulations. At later stages, this cut-off grows due to the overmerging effect.

In Fig. 9 we compare mass functions derived from the small box simulations where we expect the most reliable identification of single galactic halos. The halo masses span the range from $10^{10}M_\odot$ to $4 \times 10^{12}M_\odot$, and they can be fitted by Schechter curves of the form

$$dn/d\log M = n_*(M/M_*)^{-p} \exp(-M/M_*), \quad (6)$$

For BSI-25* we get $M_* = 10^{12}M_\odot$, $n_* = 2.6 \times 10^{-2}h^3\text{Mpc}^{-3}$

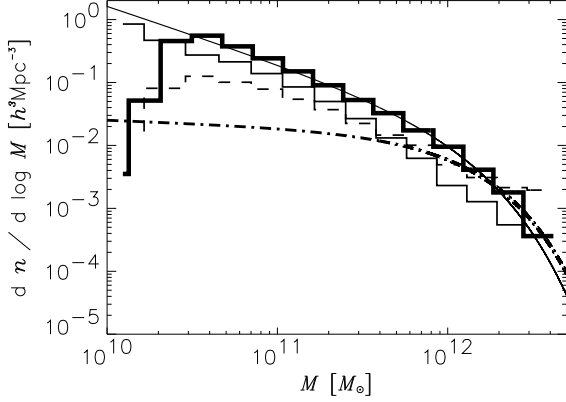


Figure 9. The ‘galaxy’ mass function of BSI-25 (thin solid histogram), of BSI-25* (thick solid histogram) compared with the CDM-25 function (dashed histogram). The solid and dash-dotted curves correspond to comparison Schechter curves with parameters provided in the text.

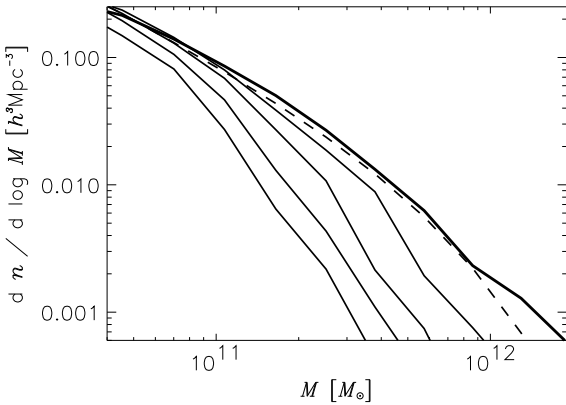


Figure 10. The halo mass function of BSI-25 at redshifts $z = 2, 1.5, 1, 0.5, 0$. For $z = 0$ a best fit Schechter distribution is shown using a characteristic mass $M_* = 6 \times 10^{11} M_\odot$, a power index $p = -1.1$ and mass density $n_* = 1.4 \times 10^{-2} h^3 \text{Mpc}^{-3}$.

and $p = 0.8$, compare the solid line in Fig. 9. The lower dashed line represents the observational results from Efsthathiou et al. (1988), $n_* = 1.6 \times 10^{-2} h^3 \text{Mpc}^{-3}$, $p = 0.1$, and also $M_* = 10^{12} M_\odot$ (assuming a quite high M/L ratio of about $100 M_\odot/L_\odot$). Similar parameters of the Schechter function are derived in Loveday et al. (1992).

The simulated mass spectra lead to approximately the same abundance of M_* galaxies as the observations. Comparison of galaxy mass spectra between CDM and BSI simulations *at the same resolution* shows that the CDM leads to a slower inclination at small masses, despite of the excessive power at small scales. Due to overmerging (Katz & White 1993; Kauffmann et al. 1993), however, we know that spectra from PM simulations may not be directly compared with observational data. One way to imagine how overmerging comes about is as follows: Potential wells associated with *galaxies* can generally bind particles with velocities of about 250 km s^{-1} . However, the potential wells in clusters can bind

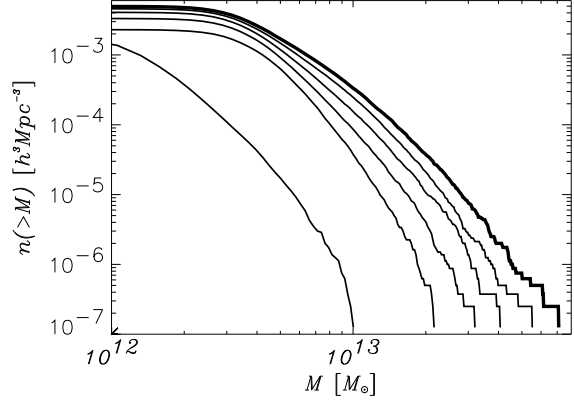


Figure 11. The cumulative halo mass function of BSI-200* at redshifts $z = 1.8, 0.67, 0.43, 0.25, 0.1, 0$. The mass range corresponds to small groups of galaxies which undergo substantial growth after $z = 1.8$.

particles with velocities of about 1000 km s^{-1} . The probability that a particle within a cluster will be near one of the deeper troughs may be slightly elevated, but not enough to distinguish galaxies, at least not using the present scheme at the presently attainable resolution. In a hydrodynamic simulation with proper treatment of cooling (Katz & Weinberg, 1992; Katz & White, 1993; and Evrard, Summers & Davis 1994), one would expect baryons to condense earlier in the galaxy (halo) potential wells, before the galaxies are assembled in the cluster. On the other hand, the PM dynamics leads to an merging of halos per se. We do not intend to make predictions on the galaxy mass functions in BSI from our simulations. We only use the halo identification scheme to get a catalog of objects with a reasonable number density, whose clustering properties should be characteristic for the primordial perturbation spectrum.

In order to understand the development of (over-) merging in a qualitative way, we studied the evolution of the mass spectra of halos (massive galaxies and groups). The redshift dependence of the differential galaxy mass function of BSI-25 is shown in Fig. 10. A Schechter fit is possible for all redshifts, only at $z = 0$ the number of very massive halos begins to exceed the exponential fall-off. Note that while the number of low-mass halos ($M < 10^{11} M_\odot$) grows by less than a factor of two between $z = 1$ and $z = 0$, the number of galaxies of $M > 5 \times 10^{11} M_\odot$ grows by a factor of about 10 or more. The redshift dependence of cumulative mass functions for BSI-200* is shown in Fig. 11. Focusing our attention on the behavior of the curves beyond $2 \times 10^{13} M_\odot$, we found an increasing of the number of high-mass halos after about $z = 0.67$, suggesting that at earlier epochs (before cluster formation), overmerging may be less severe.

Summarizing, CDM appears to lead to more massive objects than BSI (compare in Fig. 9 the thin solid and dashed lines for BSI and CDM distributions, respectively). However, in view of overmerging, the apparent disagreement of mass spectra derived in both scenarios with mass spectra inferred from luminosity functions cannot be interpreted as a weakness of either model at the present stage.

We can gain important information from the spatial

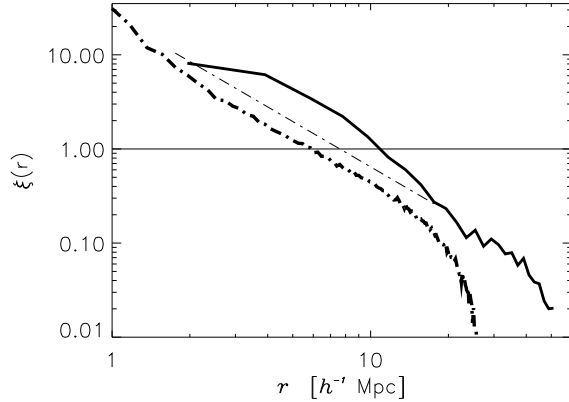


Figure 12. The correlation function of galactic halos (identified in BSI-200*, (dash-dotted line) and of cluster halos (using BSI-500, solid line). For comparison we show a straight line with slope 1.6

distribution and velocities of galaxies that are derived from our catalogs.

In Fig. 12, we show the two-point correlation function for the galaxy catalog constructed from the simulation BSI-200*. It is well described by a power law $\xi = (r/r_0)^{-\gamma}$ for $1h^{-1}\text{Mpc} < r < 15h^{-1}\text{Mpc}$, with slope $\gamma \approx 1.6$ and correlation length $r_0 \approx 6h^{-1}\text{Mpc}$. Both values are in reasonable agreement with galaxy surveys. (Because the existence of a power law for the slope of the correlation function is a quite stable property of hierarchical clustering, as demonstrated in numerous simulations, it is not a strong discriminator between models.) The slope is a bit on the shallow side, indicating that our spectrum could have a slight power deficit at galaxy scales. The correlation radius is also bit high; the halos in this galaxy catalog may be biased toward high masses and probably include small groups. Nevertheless, considering the uncertainties in identifying galaxies and the effect of overmerging, the BSI simulation results are quite compatible with observations. On the contrary, the correlation function for 'galaxies' identified in the COBE-normalized CDM simulations is much too steep (and one might expect that without overmerging it would have been even steeper). Finally, the break in the correlation function at $20h^{-1}\text{Mpc}$ and the zero crossing over $25h^{-1}\text{Mpc}$ are quite remarkable.

A robust measure of clustering is provided by the count-in-cell variances, which are volume averages of the two-point correlation function. The (mass-weighted) variance of galaxy counts in spheres of radius $8h^{-1}\text{Mpc}$ in the BSI-200 simulation is consistent with the observed variance 1. We compare the variances of galaxy and dark matter counts for spheres of different radii to get a measure of the integral bias,

$$b(r) = \sigma_{\text{gal}}(r)/\sigma_{\text{DM}}(r). \quad (7)$$

To minimize the effect of overmerging, we use in any case mass-weighted cell variances. Fig. 13 shows this bias parameter as a function of the chosen length scale. For the CDM models with more power on galactic scales, we obtain a slight antibiasing, while the bias of the BSI halos varies from 1 to 2.5, if one inspects the simulations BSI-25 to BSI-500. It should be noted that the bias factors within one simulation

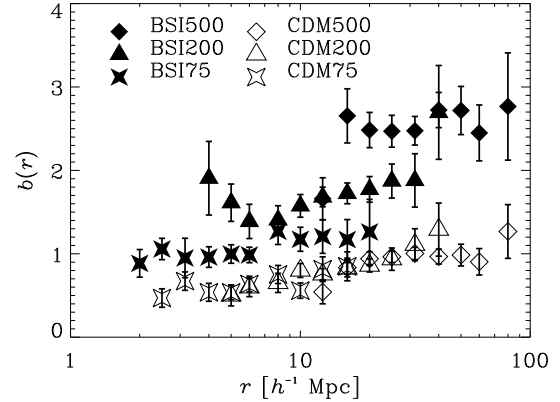


Figure 13. Integral bias of different BSI vs. CDM simulations, the error bar are $1 - \sigma$ errors estimated from the count in cell variances.

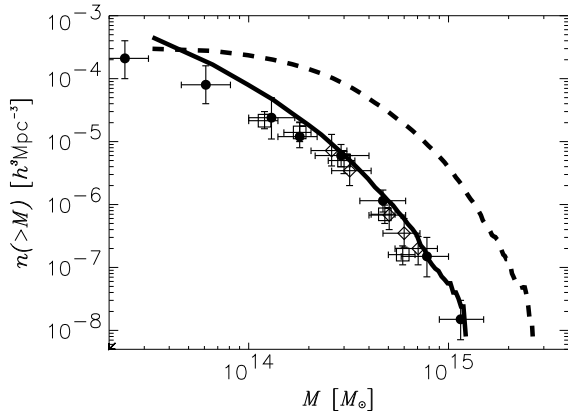
are almost constant. For deriving the counts-in-cells, we used randomly placed spheres with a total volume not exceeding the sample volume. Therefore we obtain statistically significant results. The mean errors in the cell counts are used to estimate the error bars in the 'bias' in Fig. 13. The somewhat surprising antibias of the 'peak-selected' galaxies in CDM is connected with the low threshold of the galaxy catalog used in this analysis (compare the mass functions of the galaxies). On the other hand this result is in accordance with the normalization of the corresponding simulations, the comparison of the linear theory $\sigma_{\text{DM}}(8h^{-1}\text{Mpc})$ variances, cp. Fig. 4, and the measured unit variance of galaxy counts. The results of the integral bias are summarized in Table 2.

8 ANALYSIS OF GALAXY CLUSTERS

Clusters of galaxies are widely acknowledged as a sensitive test of cosmological scenarios. Their formation is connected with the very recent decoupling of large masses from cosmic evolution. Henry and Arnaud (1991) were the first to derive restrictions on the power index of the primordial perturbation spectrum from X-ray cluster data. Using a catalog of 25 clusters with X-ray flux $L_X \geq 3 \times 10^{-11} \text{ erg cm}^{-2}\text{s}^{-1}$ (flux measured in the range 2 – 10 keV), they derived the dependence of the spatial number density on the X-ray temperature. Since the latter can be used as an indicator of the cluster mass (cp. the estimates of Evrard 1990), they obtained an estimate of the condensation probability of different mass scales. The results of Henry and Arnaud (1991) are based on the Press-Schechter (1974) theory, which supposes a Gaussian distribution of rare mass fluctuations when smoothed with a top-hat filter of the respective scale. Henry & Arnaud used in their analysis a power law spectrum $P(k) \propto k^n$ from which they obtained a spectral index $n \simeq -1.7$ ($-2.4 < n < -1.3$) at $k \simeq 0.3h \text{ Mpc}^{-1}$. This is shallower than the standard CDM model on the relevant scale (compare also Bartlett & Silk, 1993). Here we identify galaxy clusters in the largest simulations (BSI/CDM-500) using an effective search radius of $1.5h^{-1}\text{Mpc}$, the Abell radius. The resulting mass function of cluster halos is shown in Fig. 14. The observational points stem from a collection of

Table 2. Integral bias of galaxy halos

| Simulation | radii of spheres r $h^{-1}\text{Mpc}$ | mean bias $\langle b \rangle$ | standard deviation |
|------------|--|----------------------------------|-----------------------|
| BSI-200* | 5 – 40 | 1.4 | 0.2 |
| BSI-500 | 12.5 – 100 | 2.5 | 0.5 |
| BSI-200 | 5 – 40 | 1.7 | 0.4 |
| BSI-75 | 2 – 12.5 | 1.0 | 0.1 |
| BSI-25 | 0.8 – 5 | 0.8 | 0.3 |
| CDM-500 | 12.5 – 100 | 0.9 | 0.3 |
| CDM-200 | 5 – 40 | 0.8 | 0.2 |
| CDM-75 | 2 – 12.5 | 0.6 | 0.1 |
| CDM-25 | 0.8 – 5 | 0.5 | 0.2 |

**Figure 14.** The cumulative number density of cluster halos of the BSI model (solid line, BSI-500) is a good description of the data of Cen & Bahcall (1993); full dots: optical data mainly from Abell clusters; squares: X-ray observations from EXOSAT and HEAO II. CDM simulations (dashed line) significantly overproduce cluster halos.

both optical and X-ray data superimposed to get an universal empirical mass function (Cen & Bahcall 1993). The BSI-simulation fits the observational data quite well, although at $M < 6 \times 10^{13} M_{\odot}$ we see a slight overproduction of clusters. Cluster formation is a quite recent process, as Fig. 11 demonstrates. The CDM model leads to a tremendous overproduction of halos; in particular, the mass function is too steep on the cluster scale, this conclusion is typical for $\Omega = 1$ models. The break length of BSI is strongly restricted by the cluster mass function as shown by a Press–Schechter analysis (Müller 1994a).

The cluster number density is a sensitive test of the power spectrum at the transition scale between the different inflationary stages. An independent test of the power spectrum on these scales is the cluster-cluster correlation function (Bahcall & Soneira 1983, Klypin & Kopylov 1983). While the BSI correlation function, shown in Fig. 12 as a dashed line, has the correct slope, it has a comparatively small correlation radius, $r_0 \approx 10 h^{-1}\text{Mpc}$. Only slightly larger correlation radii are derived by Dalton et al. using the APM survey ($r_0 = 14.3 \pm 2.35 h^{-1}\text{Mpc}$) and by Collins et al. (1994) for a ROSAT selected cluster survey. Our estimate of $r_0 \approx 10 h^{-1}\text{Mpc}$ may be marginal consistent with the optical catalog. Of similar importance is the range of the region

of positive correlation of cluster-cluster correlation. We find from our simulation a positive cluster-cluster correlation up to at least $80 h^{-1}\text{Mpc}$. The same seems to be indicated by (up till now somewhat uncertain) observational results.

9 LARGE AND SMALL-SCALE VELOCITY FIELDS

Using catalogs of objects (large galaxies or clusters) constructed from the $200 h^{-1}\text{Mpc}$ ($M > 2 \times 10^{12} M_{\odot}$) and $500 h^{-1}\text{Mpc}$ ($M > 3 \times 10^{13} M_{\odot}$) simulations, we estimated typical bulk velocities (and standard deviations) by computing unweighted average velocities in spheres of radius R (from 2.5 to $75 h^{-1}\text{Mpc}$) centered about 512 equally spaced observers. A top-hat filter was used. (Note that with 8^3 spheres considered there is of course some overlap in the larger spheres.) The results of the $500 h^{-1}\text{Mpc}$ simulation are shown in Fig. 15. Bertschinger et al. (1990) estimated the average velocities of the mass within spheres of radius 40 and $60 h^{-1}\text{Mpc}$ centered at the Local Group as 388 ± 67 and $327 \pm 82 \text{ km s}^{-1}$, respectively (see data points in Fig. 14). At the $1\text{-}\sigma$ level, these estimates are compatible both with the BSI results and with CDM. The rms velocities for BSI-200* (not plotted) and BSI-500 are both well fitted by curves of the form $v_{\text{rms}} = v_0 \exp(-x/x_0)$, with $v_0 \approx 490 \text{ km s}^{-1}$, $x_0 = 41.7 h^{-1}\text{Mpc}$ for simulation BSI-200*, and $v_0 \approx 520 \text{ km s}^{-1}$, $x_0 = 66.7 h^{-1}\text{Mpc}$ for simulation BSI-500. The minimum mass included in the catalogs was $2.6 \times 10^{11} M_{\odot}$ for the high-resolution simulation BSI-200*, $2 \times 10^{11} M_{\odot}$ for the simulations BSI-200 and CDM-200, and $3 \times 10^{13} M_{\odot}$ for the simulations BSI-500 and CDM-500. However, varying the minimum mass had little effect (i.e., resulted in a shift well within the range of statistical uncertainty). The Lauer and Postman (1994) measurement (689 ± 178) km s^{-1} at $150 h^{-1}\text{Mpc}$ lies above the *bulk velocity* in *any* of 512 bins for all CDM and BSI simulations at the largest radius computed ($75 h^{-1}\text{Mpc}$).

An important property of BSI models as studied in GMS94 is to provide a natural mechanism for a relatively high Mach-number or “cold” flow (Ostriker & Suto 1990, Strauss et al., 1993). Small-scale velocity fields may be studied by measuring the rms line-of-sight relative peculiar velocity derived from galaxy catalogs (Turner 1976; Davis & Peebles 1983; Mo et al. 1993).

Davis and Peebles (1983) first inferred the small-scale velocity field of galaxy clustering from the anisotropy of the small-scale velocity dispersion. They derived the rms relative

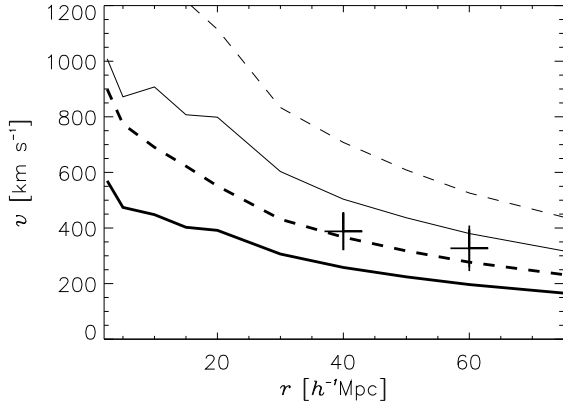


Figure 15. Streaming motions for BSI-500 (lower solid line) and CDM-500 (lower dashed line) for the largest simulation box. The thin solid line and dashed line delimit the *upper* one-sigma range obtained from different observers in the BSI-500 and CDM-500 simulation, respectively. The two error bars apply to the data from Bertschinger et al. 1990).

radial peculiar velocities $v_{\text{rms}}^2 = \langle (v_1 - v_2)^2 \rangle$ of galaxy pairs (where v_1 and v_2 are the radial peculiar velocities) as a function of the projected distance r_p between them on the sky. In the simulations we derive the relative peculiar streaming motion as function of the projected distance in bins up to $4 h^{-1}\text{Mpc}$, and the rms of the relative peculiar velocity differences for galaxies with projected separation between 1 and $2 h^{-1}\text{Mpc}$, compare Table 3. While the streaming motion falls off with increasing r , the velocity dispersion v_{rms} is almost constant, therefore we give only one value. To restrict the contamination due to foreground and background galaxies, we consider only pairs of galaxies with *real* separation less than $10 h^{-1}\text{Mpc}$. The values of the Table 3 are directly comparable to the Davis and Peebles (1983) results which give rms peculiar velocities from the apparent anisotropy of the spatial correlation function using the CfA redshift survey: $v_{\text{rms}}(R) = (340 \pm 40)(r_p h^{-1}\text{Mpc})^{0.13} \text{ km s}^{-1}$, for $r < 1 h^{-1}\text{Mpc}$. We get somewhat smaller velocity differences for all BSI simulations, which result from the combined effect of restricted power in the simulation box, and the insufficient resolution of small mass elements. In particular, we cannot resolve single galaxies in the large simulation boxes, but only infer the peculiar velocities of ‘groups’ or ‘clusters’. The highest peculiar velocities are predicted for the $75 h^{-1}\text{Mpc}$ and the high resolution $400 h^{-1}\text{Mpc}$ simulations. On the contrary, the velocity dispersion of CDM galaxies is too high.

Recent studies of the same and newer data sample seem to indicate that the small-scale velocity dispersion depends on the selection of galaxy types, especially whether large clusters are included or not (Mo et al., 1993). In the latter case, a significantly higher velocity dispersion is obtained. Also studying the groups and clusters in simulations, one gets higher rms velocities. These results do not refer to the analysis of the mean of relative velocities of *all* close projected pairs as done here.

10 CONCLUSIONS

A substantial body of independent and plausible observational evidence indicates that the primordial perturbation spectrum is not well described by the standard CDM model with Harrison-Zel’dovich primordial fluctuation spectrum. Here, we have seen that the two-parameter spectrum with broken scale invariance resulting from a double-inflationary scenario provides a good description to a substantial range of observational data: the galaxy number density, galaxy-galaxy correlations, the count-in-cell statistics of galaxies, the cluster mass and X-ray temperature functions, cluster-cluster correlations, small and large-scale velocity fields. The observed filamentary structure is evident in the galaxy distribution, the distribution of cold particles and (most prominently) in the distribution of warm ($\approx 10^6 \text{ K}$) gas.

With regard to counts in cells, the very encouraging result — obtained from the distribution of DM particles — is that the BSI simulations fit the data quite well in a wide range of scales, $[(5 - 60)h^{-1}\text{Mpc}]$. In contrast, the CDM counts in cells are inconsistent with observations at about the $2\text{-}\sigma$ level.

The variance of *galaxy* counts depends strongly on the chosen galaxy identification scheme. The results are summarized in Table 2 with the estimated integral bias. For simulations BSI-200 and BSI-200*, the results are at best typical for galactic halos, while in BSI-500 we measure instead cluster halos. In contrast, for the CDM simulations we found ‘galaxies’ that are slightly anti-biased with respect to the dark-matter distribution.

BSI seems to produce fewer massive objects than CDM. However, in view of overmerging, care must be taken in interpreting the apparent disagreement of mass spectra derived in either scenario with mass spectra inferred from luminosity functions.

The slope and correlation length of the BSI galaxy correlation function as discussed in Section 7 are close to observed values. The cluster correlation function has a correlation radius of $(10 - 15)h^{-1}\text{Mpc}$ and stays positive at least out to about $80h^{-1}\text{Mpc}$, consistent with our observational knowledge.

Rms line-of-sight velocities from BSI simulations appear to be closer to the Davis & Peebles (1983) data than comparable CDM simulations, which lie systematically too high as mentioned already in the first papers on CDM simulations.

Large-scale streaming velocities in the $500h^{-1}\text{Mpc}$ simulations are well within $1\text{-}\sigma$ statistical variations as determined from the simulations. Considering the current uncertainties in these measurements, they pose no problems for the model at this time. Moreover, a circa 25 per cent increase in the normalization as suggested by the Górski et al. (1994) reanalysis of the COBE data would suggest roughly a 7 per cent boost in typical large-scale motions at the scales in question. But in any case our predictions are much lower than the Lauer & Postman (1994) results, our BSI expectation at a scale of $150 h^{-1}\text{Mpc}$ is about 55 km/s .

An important test for the BSI spectrum will be the more precise measurement of multipole moments of the microwave anisotropy at scales of a few hundred Mpc (the Doppler peak). The advantage of these measurements is that they directly sample the linear part of the spectrum. A decisive question for BSI will be a more precise observational deter-

Table 3. First (v_{str} , defined positive inwards) and second (v_{rms}) moments of distribution of line-of-sight projected relative peculiar velocity differences of galaxy halo pairs.

| Simulation | v_{str} [km s ⁻¹] (0 - 1) $h^{-1}\text{Mpc}$ | (1 - 2) $h^{-1}\text{Mpc}$ | (2 - 3) $h^{-1}\text{Mpc}$ | (3 - 4) $h^{-1}\text{Mpc}$ | v_{rms} [km s ⁻¹] (1 - 2) $h^{-1}\text{Mpc}$ |
|------------|---|-------------------------------|-------------------------------|-------------------------------|---|
| BSI-200* | 183 | 159 | 142 | 130 | 256 |
| BSI-25* | 50 | 40 | 27 | 18 | 192 |
| BSI-500 | 176 | 169 | 139 | 106 | 243 |
| BSI-200 | 141 | 117 | 111 | 101 | 241 |
| BSI-75 | 106 | 104 | 97 | 88 | 253 |
| BSI-25 | 82 | 78 | 69 | 62 | 192 |
| CDM-500 | 362 | 373 | 316 | 266 | 469 |
| CDM-200 | 224 | 216 | 201 | 172 | 484 |
| CDM-75 | 204 | 218 | 207 | 199 | 644 |
| CDM-25 | 100 | 126 | 131 | 110 | 469 |

mination of the epoch of formation of the first objects. As mentioned in Sect. 5, improved treatment of ionization and heating processes could allow use of quasar abundance and quasar absorption line data to obtain more stringent limits on structure evolution in BSI. Of comparable importance are data expected to be available in the near future on the evolution of the cluster mass function at redshifts $z \approx 0.5$. This problem presents a theoretical challenge, because it requires an accurate hydrodynamical treatment of cluster gas dynamics in the context of large-scale structure simulations.

The most important success of the BSI scenario is the excellent agreement with present observational data on very large scale structure. In this paper, we have seen through numerical simulations that smaller scales are generally in excellent agreement with available data. In the future, it will be important to investigate additional characteristics of large-scale structure using methods such as topological studies, percolation analysis and computation of void probability functions.

In order to study mass spectra and statistics in a more reliable manner, hydrodynamic simulations should be performed. However, the results of our PM simulations strongly suggest that the BSI model studied here deserves full attention as a reliable description of cosmological structure formation.

Acknowledgements:

We would like to express our thanks to Andrei Doroshkevich and Anatoly Klypin for stimulating discussions. Our referee, David Weinberg, made a lot of constructive remarks which helped us very much in improving the paper. Karl-Heinz Böning provided invaluable support in computer management.

REFERENCES

Amendola, L., Gottlöber, S., Mückel, J. P., & Müller, V. 1995, ApJ in press
Bahcall, N. A., & Soneira, R. A. 1983, ApJS, 70, 1
Bahcall, N. A., & Cen, R. 1993, ApJ, 407, L49
Bartlett, J. G., & Silk, J. 1993, ApJ, 407, L45
Baugh, C. M., & Efstathiou, G. 1993, MNRAS 265, 145
Bertschinger, E., Dekel, A., Faber, S., Dressler, A., & Burstein, D. 1990 ApJ 364, 370

Blumenthal, G. R., Pagels, H., & Primack, J. R. 1982, Nature 299, 37
Bond, J. R., & Efstathiou, G. 1984, ApJ 285, L45
Bond, J. R., 1994, CITA-94-5 (Proceedings of the Capri meeting)
Cen, R., Gnedin, N.Y., Kofman, L. A., & Ostriker, J. 1992, ApJ 399, L11
Cen, R., Gnedin, N.Y., & Ostriker, J. 1993, ApJ 417, 387
Cen, R., & Ostriker J. 1992a, ApJ 392, 22
Cen, R., & Ostriker J. 1994, ApJ 431 451
Cen, R. 1004, ApJ 437, 12
Collins, C. A., Cruddace, R. G., Ebling, H., MacGillivray, H. T., & Voges, W. 1994 in: 'Studying the Universe with clusters of galaxies', eds. H. Böhringer, S. Schindler, MPE Report 256, 107
Davis, M., Summers, F. J. & Schlegel, D. 1992, Nature 359, 393
Davis, M. & Peebles, P.J.E. 1983, ApJ 267, 465
Doroshkevich, A. G., Fong, D., Gottlöber, S., Mückel, J. P., & Müller, V. 1995 MNRAS submitted
Efstathiou, G., Ellis, R.S., & Peterson, B.S. 1992, MNRAS 232, 431
Efstathiou, G. 1992, MNRAS 256, 43P
Efstathiou, G., Bond, J. R., & White, S. 1992, MNRAS 258, 1P
Efstathiou, G., Kaiser, N., Saunders, W., Lawrence, A., Rowan-Robinson, M., Ellis, R.S., & Frenk, C. S. 1990a, MNRAS 247, 10P
Evrard, A.E. 1990, ApJ. 363, 349
Evrard, A.E., Mohr, J.J., Fabricant, D.G., & Geller, M.J. 1993, Astr.J. 95, 985
Fall, S.M., & Rees, M. 1985, ApJ 298, 18
Fisher, K. B., Davis, M., Strauss, M. A. Yahil, A., & Huchra, J. P. 1993, ApJ 402, 44
Górski, K. M., Hinshaw, G., Banday, A. J., Bennett, C. L., Wright, E. L., Kogut, A., Smoot, G. F., & Lubin, P. 1994, ApJ 430, L89
Gottlöber, S., & Mückel, J. P. 1993, A&A 272, 1
Gottlöber, S., Mückel, J. P., & Starobinsky A. A. 1994, ApJ, 434, 417, GMS94
Gottlöber, S., Müller, V., & Starobinsky, A. A. 1991, Phys. Rev. D43, 2510 GMS91
Gottlöber, S. 1994, in: 'Studying the Universe with clusters of galaxies', Ringberg workshop, eds. H. Böhringer, S. Schindler, MPE Report 256, 79
Henry, J. P., & Arnaud, K. A. 1991, ApJ 372, 410
Kaiser, N. 1984, ApJ 284, L9
Kaiser, N. 1991, ApJ 383, 104
Kamionkowski, M., Spergel, D., & Sugiyama, N. 1994, ApJ 426, L57
Kang, H., Ostriker, J.P., Cen, R., Ryu, D., Hernquist, L., Evrard,

- A.E., Bryan, G., & Norman, M.L., 1994, ApJ 430, 83
- Kates, R., Kotok E., & Klypin, A. 1991, A& A 243, 295 (KKK91)
- Katz N., & Gunn, J. 1991, ApJ 377, 365
- Katz N., Hernquist, L. & Weinberg, D. H. 1992, ApJ 399, L109
- Katz N., & White, S. 1993, ApJ. 412, 455
- Kauffmann, G., White, S., & Guiderdoni, B. 1993, MNRAS 264, 201
- Kauffmann, G., & Charlot, S. 1994, ApJ 430, L97
- Klypin, A., Holtzman, J. Primack, J., & Regös, E. 1993, ApJ 416, 1
- Klypin, A., & Kates, R. 1991, MNRAS 251, 41P (KK)
- Klypin, A., Kates, R., & Khokhlov, A. 1992, in: 'New Insights into the Universe', Lecture Notes in Physics 171 Springer, 157 (KKK92)
- Klypin, A., & Kopylov, A. I. 1983, Soviet Astr. Letters 9, 41
- Kofman, L., Gnedin, N., & Bahcall, N. 1993, ApJ 413, 1.
- Lauer, T., & Postman, M. 1994, ApJ 425, 418.
- Lilje, P. B. 1992, ApJ 386, L33
- Loveday, J., Peterson P., Efstathiou, G., & Maddox, S. 1992, ApJ 390, 338
- Maddox, S. J., Efstathiou, G., Sutherland, W.J., & Loveday, J. 1990, MNRAS 242, 43
- Mo, H.J., Jing, Y.P., Börner, G. 1993, in: Börner & Buchert (eds.), 'Proc. 4. MPG-CAS Workshop on High Energy Physics and Cosmology' MPA/P8
- Mo, H.J., & Miralda-Escudé, J. 1994, ApJ 430, L25
- Mücket, J.P., Kates, R., Petitjean, P., & Riediger, R. 1995, in preparation
- Müller, V. 1994a, in: 'Cosmological Aspects of X-Ray Clusters of Galaxies', NATO ASI Series Vol 441, Kluwer, 439
- Müller, V. 1994, in: 'Studying the Universe with clusters of galaxies', Ringberg workshop, eds. H. Böhringer, S. Schindler, MPE Report 256, 85
- Navarro, J. F., & Benz, W. 1991, ApJ 380, 320
- Ostriker, J. 1993, Ann. Rev. Astron. Astrophys. 31, 689
- Ostriker, J., & Suto 1990, ApJ 348, 378
- Park, C., Gott, J., & da Costa, L. 1992, ApJ 392, L51
- Petitjean, P., Mücket, J. P., & Kates, R. 1995, A&A 295, L9
- Press, W. H., & Schechter, P. 1974, ApJ 187, 425
- Shapiro, P., & Struck-Marcell, C. 1985, ApJ Suppl 57, 205
- Smoot, G. F. et al. 1992, ApJ 396, 1
- Starobinsky, A. A., 1985, JETP Lettt. 42, 152
- Steinmetz, M., & Müller, E. 1995, MNRAS in press
- Thoul, A.A., & Weinberg, D.H. 1994, preprint astro-ph/941000
- Turner, E. L. 1976, ApJ 208, 20
- Vogeley, M. S., Park, C., Geller, M., & Huchra, J. P. 1992, ApJ 391, L5
- White, S., Frenk, C. S., Davis, M., & Efstathiou, S. 1987, ApJ 313, 505 MNRAS 258, 1P
- White, S., Navarro, J. F., Evrard, A. E., & Frenk, C. S. 1994, Nature 366, 429
- Zel'dovich, Y. B. 1970, A&A 5, 84